Journal of Wind Engineering & Industrial Aerodynamics 254 (2024) 105886

Contents lists available at ScienceDirect

Journal of Wind Engineering & Industrial Aerodynamics

journal homepage: www.elsevier.com/locate/jweia

Requirements for partial turbulence simulations using nondimensional turbulence energy contributions

Timothy John Acosta [a,b], Yitian Guo [a], Jin Wang [a], Stefano Brusco [a], Gregory A. Kopp [a,*]

[a] Boundary Layer Wind Tunnel Laboratory, Faculty of Engineering, Western University, London, ON, N6A 5B9, Canada
[b] University of the Philippines Diliman, Quezon City, 1100, Philippines

ARTICLE INFO

Keywords:
Partial turbulence simulation
Wind tunnel testing
Building aerodynamics

ABSTRACT

Quantifying turbulence effects is crucial for understanding building aerodynamics and for ensuring accurate wind tunnel test methods. This is especially important in wind tunnel methods that require post-experiment adjustments because approximate wind fields are used, such as the Partial Turbulence Simulation (PTS) approach. Understanding and analyzing these effects enables load adjustments since the PTS method only requires matching the high frequency portions of the upstream spectra of the longitudinal velocity component in model and full-scale. However, the limits for which the PTS method is applicable are unclear in terms of the allowable range of wind field characteristics that can be used in the wind tunnel simulation. To address this, the paper utilizes two nondimensional parameters, one representing the small-scale turbulence energy, E_S, and the other the large-scale turbulence energy, E_L, to elaborate the aerodynamic effects of turbulence intensity and integral length scales in the upstream wind. The results show that the maximum allowable mismatch ratio of integral length scales and of Jensen numbers between model and full-scale simulations depend on the target small-scale turbulence energy and the maximum allowable deviation of small-scale energy. By quantifying the effects of E_S and E_L on area-averaged pressure coefficients, the allowable limits are identified for wind tunnel test parameters that lead to negligible differences in the resultant pressure coefficient statistics in regions of separated-reattaching flow on the roof of a low-rise building.

1. Introduction

The intricate effects of turbulence on regions of separating flow are a crucial aspect of building aerodynamics and wind loading. Bearman and Morel (1983) conducted an exhaustive review of the experimental data of the time, deconstructing turbulence effects into those caused by the large-scale and the small-scale. They noted that the large scales behave quasi-statically while the small-scales affect the local flow around the body and control the aerodynamic coefficients. The Partial Turbulence Simulation (PTS) method of wind tunnel testing relies on this distinction such that the longitudinal power spectral densities, S_u, in the high frequency range must be matched in model and full-scale

$$\frac{f_1 S_{u1}(f_1)}{\overline{u}_1^2} = \frac{f_2 S_{u2}(f_2)}{\overline{u}_2^2} \tag{1}$$

where f is the frequency, $\overline{u}$ is the mean wind speed, and the subscripts '1' and '2' are for full scale and model scale, respectively. Irwin (2008) was the first to utilize this for buildings, with a particular focus on the region of separated-reattaching flow on low-rise building roofs. However, this concept has been used in bridge aerodynamics for section model testing going back much earlier (e.g., Irwin, 1998; Macdonald et al., 2002). Detailed research on PTS methods for buildings can be found in many papers, although these all tend to focus on roofs or rooftop equipment on low-rise buildings (e.g.,Asghari-Mooneghi et al., 2016; Banks, 2011, 2013; Moravej et al., 2018; Braun et al., 2021; Estephan et al., 2022). Wind tunnel test standards such as ASCE 49-21 (ASCE, 2021) allow this method to be used. Kopp (2023) indicates that there are three constraints for PTS to work: (1) Quasi-steady theory must hold at the low-frequencies/large-scales of the wind turbulence to allow for correction for different integral scales; (2) The high frequencies must match the targets as indicated by Eq. (1) over the range appropriate for the aerodynamic mechanisms (e.g., $0.1 < \frac{fH}{\overline{u}} < 1$ for separated-reattaching flow above a low-rise building roof); and (3) The reduced turbulence intensity does not alter the aerodynamic mechanism.

* Corresponding author.
E-mail address: gakopp@uwo.ca (G.A. Kopp).

https://doi.org/10.1016/j.jweia.2024.105886
Received 1 June 2024; Received in revised form 27 August 2024; Accepted 7 September 2024
Available online 17 September 2024

Despite the extensive research done to date, there is still uncertainty around the precise limits of cut-off frequencies and allowable integral scales in the approach flow, as discussed in Kopp (2023). For example, ASCE 49-21 requires $L_u/H \geq 3$, although its Commentary indicates that the method may be useful for L_u/H in the range of 0.7–1.5. However, it is not clear how such experiments could be achieved given the required simulation frequencies for Eq. (1) in the range $0.1 < fH/\overline{u} < 1$.

For regions of separated-reattaching flow on building surfaces, Morrison and Kopp (2018) found that the nondimensional frequency range, $0.1 < fH/\overline{u} < 2$, within the upstream wind spectra as crucial in controlling flow separation and reattachments. This range, which they termed the "active scales" of turbulence, delineates where the energy in the building surface pressure spectra nonlinearly responds to the wind turbulence energy, significantly influencing the dynamics of the separated shear layer and altering the reattachment length. Their experiments showed that there needs to be sufficient turbulence energy in this range of frequencies for the characteristic high peak suctions to occur near the building edge. When turbulence energy in this range of frequencies is relatively low, the highest fluctuations instead occur near the reattachment point, which is also extended further from the roof edge, leading to entirely different loading patterns.

One of the aspects of the building aerodynamics that could support a possibly greater range of flow simulations for PTS is based on the observation of Wu and Kopp (2018) that area-averaged pressure coefficients obtained by the quasi-steady vector model do not depend significantly on the terrain conditions once the aerodynamic roughness length is sufficiently large. Certainly, within the range of open country to suburban terrain, they observed this to hold. Using detailed flow field measurements within and around the separation bubbles together with simultaneous surface pressure measurements, Akon and Kopp (2018) concluded that the effects of upstream turbulence on the flow separation mechanisms become saturated, leading to the unchanging aerodynamic coefficients observed by Wu and Kopp (2018). These facts indicate that PTS may not need to follow Eq. (1) precisely, allowing for additional testing possibilities while still allowing for accurate aerodynamic coefficients to be obtained. The objective of this paper is to develop a framework to examine this point.

To achieve this objective, this paper introduces nondimensional parameters to quantify the effects of large- and small-scale turbulence energy on pressure fluctuations in separated-reattaching flow regions. The analysis framework focuses on assessing turbulence effects on peak pressure components, including means, standard deviations, and peak factors, by examining different wind tunnel experiments of the Texas Tech University (TTU) building by Levitan and Mehta (1992a, b). Applying a quasi-steady assumption and pressure decomposition, the study quantifies trends in large-scale energy effects on low-frequency pressure fluctuations and small-scale energy effects on high-frequency pressure fluctuations. Specifically, the paper aims to identify the maximum allowable change in small-scale energy to ensure negligible differences in mean values, standard deviations, and peak factors. Recommendations for maximum allowable mismatches in integral length scales and turbulence intensity are provided based on target full-scale metrics, delineating turbulence limits where PTS remains applicable.

2. Proposed theoretical framework

2.1. Nondimensional wind energy contribution

The von Karman model for longitudinal wind spectra is

$$\frac{fS_u}{\sigma_u^2} = \frac{4\left(\frac{fL_u}{\overline{u}}\right)}{\left[1 + 70.8\left(\frac{fL_u}{\overline{u}}\right)^2\right]^{5/6}} \tag{2}$$

where f is the frequency, S_u is the longitudinal power spectral density, σ_u^2 is the variance of the wind velocity, L_u is the integral length scale, and $\overline{u}$ is the mean wind speed. This model can be renormalized as

$$\frac{fS_u}{\overline{u}^2} = \frac{4I_u^2\left(\frac{fL_b}{\overline{u}}\right)\left(\frac{L_b}{L_u}\right)^{2/3}}{\left[\left(\frac{L_b}{L_u}\right)^2 + 70.8\left(\frac{fL_b}{\overline{u}}\right)^2\right]^{5/6}} \tag{3}$$

Equation (3) allows one to parametrically investigate the effects of turbulence intensity, I_u, and normalized integral length scales, L_u/H, on the power spectral density, using $L_b = H$ (roof height) for low-rise buildings. Using Eqn. (3) one can quantify the degree to which turbulence intensity shifts the spectra vertically and the degree to which integral length scales shift the spectra horizontally. Similarly, a model can be derived to study the effects of lateral and vertical turbulence. The model can be written as

$$\frac{fS_\varepsilon}{\overline{u}^2} = \frac{4I_\varepsilon^2\left(\frac{fH}{\overline{u}}\right)\left(\frac{H}{L_\varepsilon}\right)^{2/3}\left[\left(\frac{H}{L_\varepsilon}\right)^2 + 755.2\left(\frac{fH}{\overline{u}}\right)^2\right]}{\left[\left(\frac{H}{L_\varepsilon}\right)^2 + 283.2\left(\frac{fH}{\overline{u}}\right)^2\right]^{11/6}} \tag{4}$$

where L_ε is the integral length scales and I_ε is the turbulence intensity, with the subscript, ε, referring either to the lateral, v, or vertical, w, direction.

To examine the effects of turbulence parameters on high-frequency wind fluctuations, the corresponding contribution to the small-scale energy scales, E_s, is

$$E_S = \int_{n_c}^{\infty} \frac{4I_u^2\left(\frac{fH}{\overline{u}}\right)\left(\frac{H}{L_u}\right)^{2/3}}{\left[\left(\frac{H}{L_u}\right)^2 + 70.8\left(\frac{fH}{\overline{u}}\right)^2\right]^{5/6}} d\left(\frac{fH}{\overline{u}}\right) \tag{5}$$

where n_c is the non-dimensional cut-off frequency limit. Theoretically, Eqn. (5) is integrated from $n_c = 0.1$ to ∞ since high frequency fluctuations can be defined as being $n_c = fH/\overline{u} > 0.10$. A practical limit of $fH/\overline{u} = 2$, instead of infinity, is applied for the definition of E_S. This range of nondimensional frequencies coincides with the active range (Morrison and Kopp, 2018). Similarly, the contribution to low-frequency energy scales, E_L, is

$$E_L = \int_{0}^{n_c} \frac{4I_u^2\left(\frac{fH}{\overline{u}}\right)\left(\frac{H}{L_u}\right)^{2/3}}{\left[\left(\frac{H}{L_u}\right)^2 + 70.8\left(\frac{fH}{\overline{u}}\right)^2\right]^{5/6}} d\left(\frac{fH}{\overline{u}}\right) \tag{6}$$

which covers the quasi-steady range of frequencies. The terms E_S and E_L represent the integrated area of the nondimensional spectra. These terms allow us to attribute a difference in the aerodynamics to a single value (integrated area) rather than a spectral point or line. Physically, E_S and E_L represent the contribution of high and low-frequency fluctuations to the total pressure variance, $\sigma_{C_p}^2$. This is also convenient for capturing differences in the turbulence energy for different wind tunnel test configurations.

2.2. Partial turbulence simulation theory

Fig. 1a illustrates the usual scenario for partial turbulence simulation wherein the energy in the high-frequencies matches but the low-frequency turbulence scales do not (Irwin, 2008), as required by Eq. (1). The total small-scale energy for both sets of turbulence parameters (E_{S1}, E_{S2}) are shown as the yellow area below the curve. Thus, mathematically speaking,

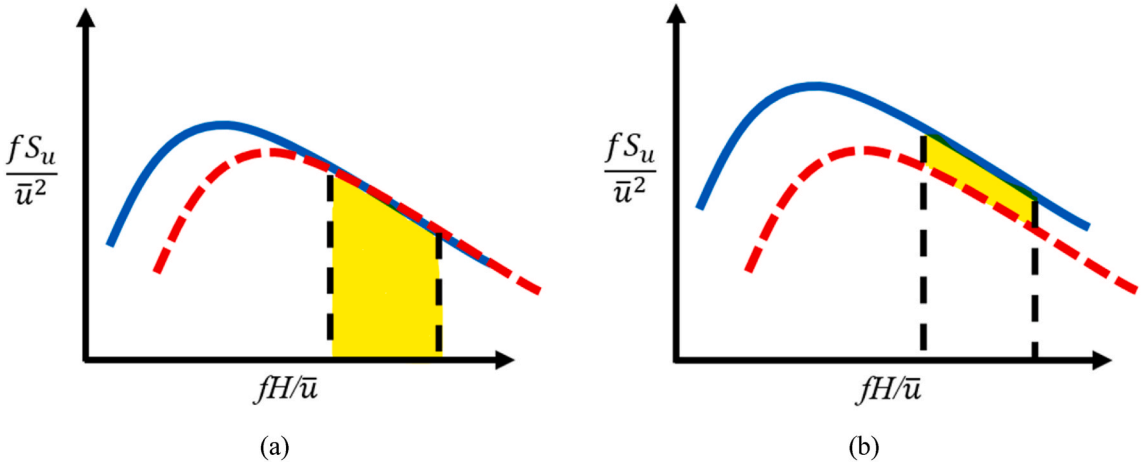

Fig. 1. Illustrations of wind spectra (a) with matching small-scale energy, $E_{S1} = E_{S2}$, (b) with a maximum allowable deviation of small-scale energy, $\Delta E_{S,max}$.

$$E_{S1} = E_{S2} \tag{7}$$

for the same non-dimensional frequency range. Substituting Eqn. (5) into Eqn. (7) results in

$$\int_{n_c}^{\infty} \frac{4I_{u1}^2(\eta)\left(\frac{H_1}{L_{u1}}\right)^{2/3}}{\left[\left(\frac{H_1}{L_{u1}}\right)^2 + 70.8(\eta)^2\right]^{5/6}} d(\eta) = \int_{n_c}^{\infty} \frac{4I_{u2}^2(\eta)\left(\frac{H_2}{L_{u2}}\right)^{2/3}}{\left[\left(\frac{H_2}{L_{u2}}\right)^2 + 70.8(\eta)^2\right]^{5/6}} d(\eta) \tag{8}$$

where $\eta = fH/\bar{u}$. Neglecting $(H_1/L_{u1})^2$ and $(H_2/L_{u2})^2$ in the denominator of both sides of Eqn. (8) leads to a negligible difference in their corresponding E_S values such that these terms can be neglected. Simplifying the equation leads to

$$I_{u1}^2 \frac{H_1^{2/3}}{L_{u1}^{2/3}} \int_{n_c}^{\infty} \frac{\eta}{\eta^{10/6}} d(\eta) = I_{u2}^2 \frac{H_2^{2/3}}{L_{u2}^{2/3}} \int_{n_c}^{\infty} \frac{\eta}{\eta^{5/3}} d(\eta) \tag{9}$$

Eqn. (9) implies that the similarity of small-scale energy between two different spectra are controlled by I_u and L_u/H. This can be simplified to

$$\frac{I_{u1}}{I_{u2}} = \left(\frac{H_2}{H_1}\right)^{1/3} \left(\frac{L_{u1}}{L_{u2}}\right)^{1/3} \tag{10}$$

since the integral terms cancel. This was first derived by Irwin (1998) by satisfying Eq. (1).

Using the concept of E_s, the difference in the variance between two wind spectra, ΔE_s, for two different sets of turbulence parameters (I_u,L_u/H) can be quantified. This concept is illustrated in Fig. 1b, wherein the yellow area corresponds to the difference in small-scale energy over the active range. Mathematically, this can be expressed as

$$\Delta E_s = E_{S1} - E_{S2} \tag{11}$$

Substituting Eqn. (5) into Eqn. (11) yields

$$\Delta E_s = \int_{n_c}^{\infty} \frac{4I_{u1}^2(\eta)\left(\frac{H_1}{L_{u1}}\right)^{2/3}}{\left[\left(\frac{H_1}{L_{u1}}\right)^2 + 70.8(\eta)^2\right]^{5/6}} d(\eta) - \int_{n_c}^{\infty} \frac{4I_{u2}^2(\eta)\left(\frac{H_2}{L_{u2}}\right)^{2/3}}{\left[\left(\frac{H_2}{L_{u2}}\right)^2 + 70.8(\eta)^2\right]^{5/6}} d(\eta) \tag{12}$$

Again, neglecting $(H_1/L_{u1})^2$ and $(H_2/L_{u2})^2$ in the denominator and simplifying Eqn. (12) leads to

$$\Delta E_s = \left[\frac{I_{u1}^2 H_1^{2/3}}{L_{u1}^{2/3}} - \frac{I_{u2}^2 H_2^{2/3}}{L_{u2}^{2/3}}\right] \int_{n_c}^{\infty} \frac{4\eta}{70.8\eta^{5/3}} d(\eta) \tag{13}$$

Eqn. (13) enables one to determine the difference in small-scale energy considering the turbulence intensity and integral length scales. Using this concept, a maximum allowable deviation of small-scale energy, $\Delta E_{s,max}$, can be defined such that the effects of the change in small-scale energy on the aerodynamic mechanisms are minimal. Here, the magnitude of $\Delta E_{s,max}$ is defined based on quantifying the effects of E_S on the separation bubble above a low-rise building. Limiting the integration from $0.1 \le \eta \le 2.0$, Eqn. (13) can be simplified to

$$I_{u2}^2 \left(\frac{H_2}{L_{u2}}\right)^{2/3} = I_{u1}^2 \left(\frac{H_1}{L_{u1}}\right)^{2/3} - 7.41\Delta E_{s,max}. \tag{14}$$

Eqn. (14) allows one to determine a set of turbulence parameters that will have similar aerodynamics given that the difference between two small-scale energies is less than $\Delta E_{s,max}$.

2.3. Application to ASCE 49-21 provisions

ASCE 49-21 (2021) requires that

$$\left(\frac{L_u}{L_b}\right)_m = \left(\frac{L_u}{L_b}\right)_p \tag{15}$$

where the subscript m and p refers to the model scale and prototype (i.e., full scale), respectively. In consideration of full-scale uncertainties, the ASCE 49-21 allows Eqn. (15) to have an allowable mismatch of integral length scales by a factor of 3 but with the minimum integral length scales, $L_u/H > 3$. However, the provisions are silent on how to treat the turbulence intensity in the scenario of an integral scale mismatch. Fig. 2a illustrates a scenario where the turbulence intensity is constant but with a mismatch of integral length scale such that the energy in the active scales is also altered. Considering Eqn. (14), the turbulence intensity may be factored out and be re-written as

$$\Delta E_{s,max} = \left[\left(\frac{H_1}{L_{u1}}\right)^{2/3} - \left(\frac{H_2}{L_{u2}}\right)^{2/3}\right] \frac{I_u^2}{7.41}. \tag{16}$$

Defining $\alpha = (L_u/H)_2 / (L_u/H)_1$, where α is the factor quantifying the mismatch between two sets of integral length scales, and eliminating the subscript "2" for the integral length scales results in

$$\alpha = \left(7.41 \frac{\Delta E_{s,max}}{I_u^2} \left(\frac{L_u}{H}\right)^{\frac{2}{3}} + 1\right)^{3/2} \tag{17}$$

Eqn. (17) allows one to relate the mismatch in integral length scales to the maximum allowable mismatch in small-scale energy, $\Delta E_{s,max}$, where L_u/H now refers to the target integral length scale ratio."

In addition to the requirement of the matching of the integral length

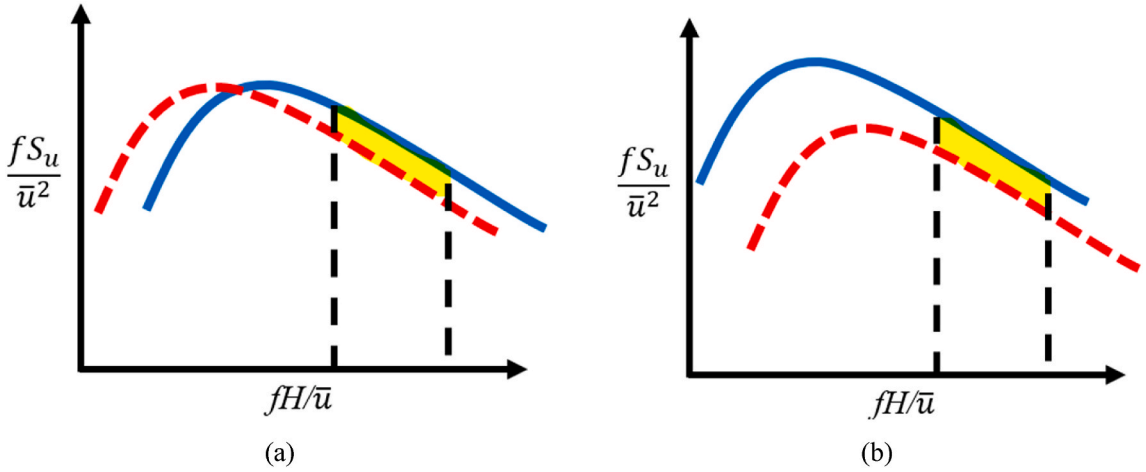

Fig. 2. Illustrations of wind spectra maximum allowable deviation of small-scale energy (a) due to a mismatch of integral length scales, L_u/H and (b) due to a mismatch of the Jensen number, H/z_o.

scales, ASCE 49-21 requires Jensen number matching,

$$\left(\frac{L_b}{z_o}\right)_m = \left(\frac{L_b}{z_o}\right)_p \tag{18}$$

where z_o is the roughness length. An allowable mismatch by a factor of three is allowed in ASCE 49-21. Similar to the analysis on the integral length scales, a mismatch of the Jensen number, and its corresponding effects on the small-scale energy, can be evaluated. The roughness length, z_o, can be related to turbulence intensity and integral length scales by the ESDU 74 (ESDU, 1975) recommendations. Then, a corresponding mismatch factor for the Jensen number, $\alpha_{zo} = (H/z_o)_1 / (H/z_o)_2$, can be evaluated as a function of $\Delta E_{s,max}$ and z_o. Fig. 2b illustrates a scenario where there is a mismatch of the Jensen number, which translates to a vertical shift of the spectra due to a mismatch in turbulence intensity and a horizontal shift of the spectra due to a mismatch in integral length scales.

In this paper, an example of quantifying the limits $\Delta E_{s,max}$, α, and α_{zo} such that the aerodynamic loads for the separated flow above a low-rise building are not significantly altered. The results, considering data for the TTU building, are examined in Section 4. It is also noted that this framework may be extended to quantify $\Delta E_{s,max}$ for other body-generated vortices (e.g., horseshoe vortex, vortex shedding), although further work is required to understand these (Kopp, 2023).

2.4. Quantifying maximum allowable deviation of small-scale energy

The magnitude of $\Delta E_{s,max}$ should be defined based on having minimal effects on parameters of interest, μ_i, related to the peak pressure coefficients. A common method to decompose the peak pressure coefficient is given by

$$\hat{C}_p = \bar{C}_p + g_{Cp}\sigma_{Cp} \tag{19}$$

where $\bar{C}_p$ is the mean pressure coefficient referenced to the mean dynamic wind pressure at roof eave height, g_{Cp} is a peak factor, and σ_{Cp} is the rms pressure coefficient. Assuming a linear variation of the parameter of interest, μ_i, for a small increment of small-scale energy, the maximum allowable deviation of small-scale energy can be defined by limiting the difference of the parameter of interest. The validity of this assumption, particularly for nondimensional pressure energy, will be shown in Section 4.3. In order to ensure that relative differences are not associated with aerodynamic behavior. We propose that the limit for any parameter interest not be greater than measurement uncertainty limits. The relative difference is set at 15% for this paper, which Kwan and Kopp (2021) recommend as the uncertainty bounds for wind tunnel experiments similar to those considered herein. Mathematically, this maximum allowable difference can be set as

$$\Delta E_{S,max} = \frac{0.15\mu_i}{d\mu_i/dE_S} \tag{20}$$

For the separated flow above the roof of a low-rise building, the effects of small-scale energy on each parameter, μ_i, are highly dependent on the location of the pressure measurement. Thus, the slope, $d\mu_i/dE_S$, is dependent on the location of the pressure measurement. Additionally, the effects of small-scale turbulence on the fluctuations of point pressure and area-averages may differ significantly (Kopp, 2023). Therefore, $\Delta E_{S,max}$ is investigated for different point pressure locations and for different area-averages on the roof.

2.5. Mean pressure field

It is well known that the mean pressure field correlates well with the upstream turbulence for the pressure coefficients under the separation bubble on the roof of low-rise buildings (Akon and Kopp, 2016; Wu et al., 2017). Guo et al. (2021) used the small-scale portion of the upstream turbulence kinetic energy as a proxy to account for the mechanisms in the region of separated flow. Similar to Guo et al. (2021), we propose that E_S may be used as a proxy to account for the contribution of the Reynold's normal stresses component, $\overline{u'u'}/\overline{u^2}$, to the total mean pressure gradient, where the prime corresponds to fluctuating components. Wu et al. (2017) showed that $\overline{u'u'}/\overline{u^2}$ dominates the stress tensor, having four times the magnitude of $\overline{u'w'}/\overline{u^2}$ and $\overline{w'w'}/\overline{u^2}$, where w' refers to the vertical component of fluctuations. Thus, we examine how the minimum pressure coefficient, $\bar{C}_{p,min}$, along the centerline of the roof, the location of this minimum with respect to the leading edge, x_{min}/H, and the reattachment length, x_r/H, vary with respect to E_S. These three parameters derived from the surface mean pressure field are important indicators on how the separation bubble changes with respect to turbulence (Akon and Kopp, 2016, Wu et al., 2017). The reattachment lengths, x_r/H, for the current study were approximated using the model of Akon and Kopp (2016). Aside from these parameters, Roshko and Lau (1965) used a reduced pressure coefficient Cp*

$$C_p^* = \frac{(\bar{C}_p - \bar{C}_{p,min})}{(1 - \bar{C}_{p,min})} \tag{21}$$

and discussed that the mean pressure measurements are highly correlated in this normalized form. Thus, we empirically examine how Cp* is affected by E_S in section 4.2.

2.6. Nondimensional pressure energy

The effects of E_S and E_L on the pressure variance are examined by applying the quasi-steady assumption. The influence of E_S on high-frequency pressure fluctuations is investigated by decomposing the pressure signal into low and high-frequency fluctuations in the frequency domain. Likewise, the impacts of E_L on the low-frequency pressure fluctuations are determined. The quasi-steady theory allows us to relate the pressure signal to a longitudinal upstream velocity signal by

$$S_{Cp}(f) = 4\frac{\overline{C}_p^2}{\overline{u}^2}S_u(f)\chi^2(f) \tag{22}$$

where S_{Cp} is the power spectral density of the pressure signal, and $\chi^2(f)$ is the aerodynamic admittance function. By renormalizing the pressure spectra, a relationship to normalized wind spectra can be derived as

$$\frac{fS_{Cp}(f)}{\overline{C}_p^2} = 4\frac{fS_u(f)}{\overline{u}^2}\chi^2(f) \tag{23}$$

Equation (23) allows one to visualize how turbulence intensity and integral length scales parametrically affect the pressure spectra. By using Eqns. (3), (5) and (6) with Eqn. (23), the nondimensional pressure energy for low frequency and high frequency pressure fluctuations can be written as

$$E_{PL} = 4E_L\beta_L \tag{24}$$

$$E_{PS} = 4E_S\beta_S \tag{25}$$

respectively, where E_{PL} is the nondimensional energy of the low frequency pressure fluctuations, E_{PS} is the nondimensional energy for high-frequency pressure fluctuations, and β_L and β_S are factors that consider the integrated effects of the admittance function for low frequency and high frequency pressure fluctuations, respectively. The terms β_L and β_S allows one to use a single value to examine how the admittance changes for different building surfaces of interest. Fig. 3 visually illustrates the relationship between the proposed nondimensional energy for the velocity and pressure fluctuations defined by Eqns. (24) and (25). For cases where quasi-steady theory holds perfectly, the admittance is constant at one for $0 < \eta \leq 0.1$, resulting in $\beta_L = 1.0$. For cases where body-generated turbulence effects are significantly present on the roof, the admittance is smaller or larger than one (Wang and Kopp, 2023), i.e., $\beta_S \neq 1.0$, depending on the body-generated details.

2.7. Peak factors

The effects of the nondimensional wind energy on the peak factor are examined by investigating parameters that theoretically affect it. It is well known that peak factors for regions of separated flow are non-Gaussian (Ginger and Letchford, 1993; Kareem and Wu, 2013; Wang and Kopp, 2023). A common method for determining non-Gaussian peak factors is by using the translation framework of Rice (1945). The CDF mapping method is a translation framework that is known to perform well (Grigoriu, 1995; Sadek and Simiu, 2002; Peng et al., 2014; Zhao et al., 2019; Acosta et al., 2024). Therefore, the non-Gaussian peak factor can be determined as

$$g_{Cp} = F_X^{-1}\left(\Phi\left(\sqrt{2\ln\frac{v_o T}{\ln(1/p)}}\right)\middle|\theta_i\right) \tag{26}$$

where $F_X(.)$ is the CDF of the pressure signal with distribution parameters θ_i, v_o is the up-crossing rate, T is the time interval, and p is the target probability of exceedance. In Eqn. (26), the two main parameters that are affected by the nature of the flow mechanisms are the Gaussian crossing rate and the empirical statistical distribution of the pressure fluctuations. Hence, we examine the effects of E_S and E_L on these two parameters to examine implicitly how the non-Gaussian peak factor is affected.

2.7.1. Crossing rates

The Gaussian crossing rate can be determined by

$$v_o = \sqrt{\frac{\int_0^\infty f^2 S_{Cp}(f).df}{\int_0^\infty S_{Cp}(f).df}} \tag{27}$$

The non-Gaussian up-crossing rate is approximated using Eqn. (27). This assumption is acceptable because the differences associated with using a Gaussian crossing rate lead to a negligible difference in the peak pressures (Grigoriu, 1995; Sadek and Simiu, 2002). To investigate the effects of the wind spectra on the contributions to a normalized crossing rate, Eqn. (27) can be renormalized as

$$\frac{v_o^2\sigma_{Cp}^2}{\overline{u}^2} = \int_0^\infty \frac{fS_u(f)}{\overline{u}^2}\chi^2(f)f.df \tag{28}$$

The low and high-frequency components of the renormalized

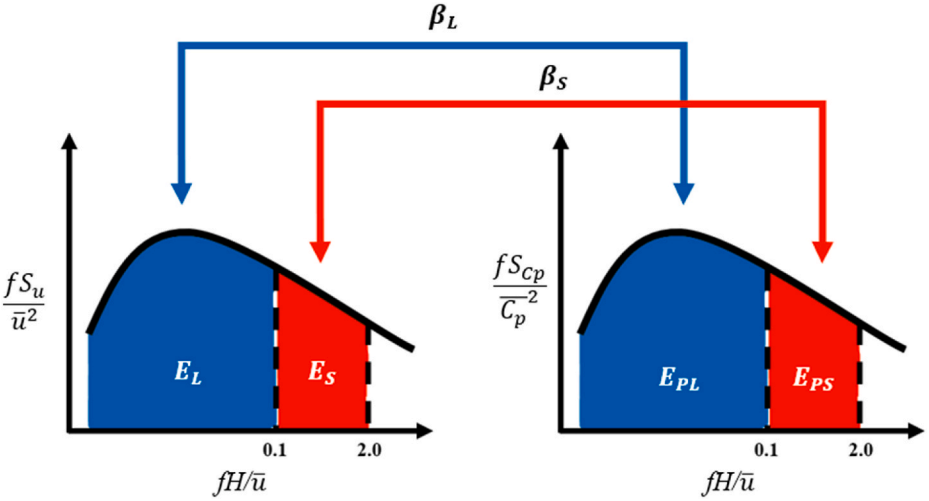

Fig. 3. Illustrations of the relationship of nondimensional energy between wind and pressure fluctuations for low and high-frequency fluctuations.

Gaussian crossing rate can then be expressed as

$$\left(\frac{v_o^2\sigma_{Cp}^2}{\overline{u}^2}\right)_L = \int_0^{n_c} \frac{fS_u(f)}{\overline{u}^2}\chi^2(f)f.df \tag{29}$$

and

$$\left(\frac{v_o^2\sigma_{Cp}^2}{\overline{u}^2}\right)_S = \int_{n_c}^{\infty} \frac{fS_u(f)}{\overline{u}^2}\chi^2(f)f.df \tag{30}$$

respectively. Using Eqn. (29) and Eqn. (30), the contribution of low and high energy scales of the upstream wind spectra to the Gaussian crossing rate can be examined.

2.7.2. Statistical distributions

Aside from the effects on the crossing rate, it is essential to understand the effects of small- and large-scale energy on the statistical distribution of pressure fluctuations. The pressure time signal is decomposed into low and high frequency time signals using the Quasi-steady (QS) vector model (Wu and Kopp, 2016, 2018; Guo et al., 2021). The low-frequency pressure time signal, p_L, is

$$p_L(t) = \frac{1}{2}\rho V_S(t)^2 C_p(\theta,\beta) \tag{31}$$

where ρ is the density, V_S is the filtered time-varying velocity magnitude, and $C_p(\theta,\beta)$ is the quasi-steady pressure coefficient, which is a function of azimuth, θ, and elevation angle, β. The filtered velocity is obtained using a sine-weighted frequency filter (Tubino and Solari, 2020) and takes the form

$$V_S(t)^2 = \sum_{j=1}^{3} u_{j,s}(t)^2 \tag{32}$$

where $u_{j,s}$ are the filtered velocity components determined by

$$u_{j,s}(t) = \sum_{i=1}^{N} u_j(i)W(t - i \bullet \Delta t) \tag{33}$$

where u_j are the original velocity components, W is the weighting function, and Δt is the time step size, which is the inverse of the sampling rate, f_s. The sine-weighted filter is determined as

$$W(t) = \frac{\sin\left(\frac{2\pi t}{n_c}\right)}{\pi t} \tag{34}$$

The corresponding high-frequency pressure time signal, p_S, is then determined by

$$p_S(t) = p(t) - p_L(t) \tag{35}$$

Using this pressure decomposition framework, the peak factor can be derived as

$$g_{Cp}(t) = \frac{\left(C_{p,L}(t) + C_{p,S}(t)\right) - \overline{C}_p}{\sigma_{Cp}} \tag{36}$$

where the contribution of the low and high-frequency pressure fluctuation to the instantaneous peak factor can be determined by

$$g_{Cp,L}(t) = \frac{C_{p,L}(t) - \overline{C}_p}{\sigma_{Cp}} \tag{37}$$

and

$$g_{Cp,S}(t) = \frac{C_{p,S}(t)}{\sigma_{Cp}} \tag{38}$$

respectively. The skewness and kurtosis of the pressure time series as a function of the upstream turbulence energy can then be examined.

3. Experimental setup

The experiments were conducted in the Boundary Layer Wind Tunnel II at Western University. The building model has plan dimensions of 27.5 cm × 18.3 cm (B × L) with an eave height of 7.8 cm (H). In this study, the effects on the pressure fluctuations for four corner panel configurations with four (C-4), nine (C-9), sixteen (C-16), and thirty-six (C-36) pressure taps are investigated. Each panel location is shown in Fig. 4. Additionally, the wind direction perpendicular to the breadth, B, is considered in this study and shown in Fig. 4. The effects of turbulence on selected point pressures near the leading edge (LE), at the center of the roof (CN), and the trailing edge (TE) are also examined. A sampling rate of 625 Hz with a total sampling duration of 180 s was utilized for the pressure and velocity signals. The details of the pressure measurement system may be found in Ho et al. (2005).

Six different terrain categories were simulated for a TTU model with a length scale of 1/50. The simultaneous wind velocity was measured using a Cobra probe at the roof eave height (H), 2H upstream, and an adjacent distance of 3H from the building side. Although there is a reduced correlation between the velocity and pressure signal at an adjacent distance of 3H from the building side (Wu et al., 2017), this location was chosen (at roof eave height) to have comparable energy levels with full-scale measurements of the TTU building (Levitan and Mehta, 1992) and the experiments of Morrison and Kopp (2018), which were referenced at roof height. The corresponding power spectral density for the upstream velocity signal of the six terrain cases are shown in Fig. 5 while the relevant wind characteristics are found in Table 1. Further details can be found in Wu and Kopp (2018).

4. Results & discussion

4.1. Nondimensional small-scale energy application to PTS

As discussed in the Introduction, for PTS to be accurate Kopp (2023) briefly discusses three restrictions. First, the quasi-steady theory must hold in order to correct for the low-frequency fluctuations. Second, the active scales of energy should be properly simulated. Third, the difference in the upstream turbulence between a model and a full-scale test should not result in significant differences in the aerodynamic mechanisms.

Fig. 6 depicts the target small-scale energy as a function of the turbulence intensity and integral length scale ranges that can be simulated in a typical atmospheric boundary layer wind tunnel. This allows one to consider the applicable pair of turbulence parameters given the constraints of the geometry of a specific wind tunnel set-up, which will dictate the maximum integral length scales (Stathopoulos and Surry, 1983). It is important to note that for low levels of turbulence intensity, such as $I_u = 0.10$, an increase in integral length scales from 6 to 13 reduces the small-scale energy by about $\sim 4 \times 10^{-4}$, which is a negligible shift in energy. On the other hand, an increase in the integral length scales of the same magnitude for a high level of turbulence intensity such as 0.30 would result in the small-scale energy shifting by $\sim 3 \times 10^{-3}$- an order of magnitude higher than the case with a lower turbulence intensity. This implies that significant integral length scale effects on building aerodynamics may not be observed in lower turbulence levels. Additionally, as noted in the Introduction, Akon and Kopp (2018) concluded that upstream turbulence effects on the separating shear layer may saturate. Although larger integral length scales may significantly increase the small-scale energy when there is higher turbulence intensity, the saturation effects of turbulence prevent a significant change in the mechanisms controlling the separating shear layer. Clearly, it is essential to determine the limits of E_S such that small-scale energy effects lead to minimal changes in the aerodynamics in order to establish the range where integral length scales effects will be apparent.

The objective here is to determine the limits of mismatches in small-

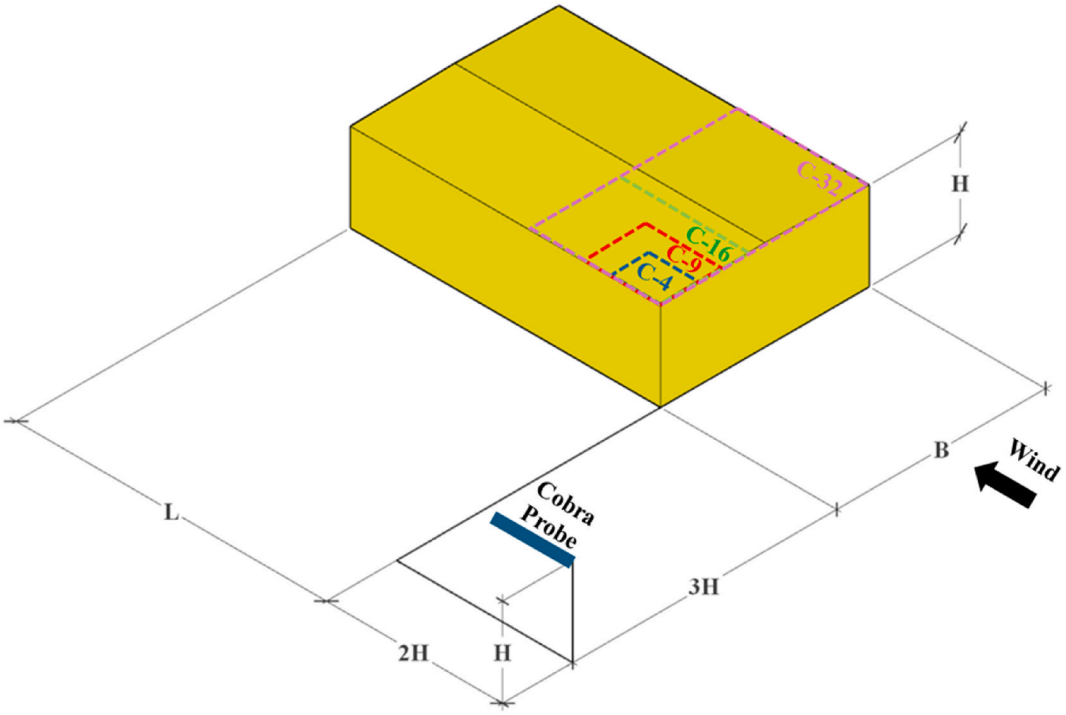

Fig. 4. Experimental setup indicating four panel configurations, three point pressure locations on the roof of the model and the location of the cobra probe with respect to the building model and wind direction.

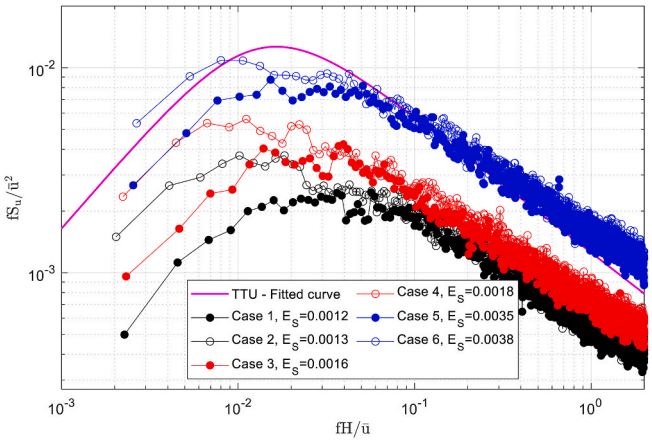

Fig. 5. Power spectral density and small-scale energy for the six terrains in model scale and full-scale terrain conditions.

scale energy, $\Delta E_{S,max}$, which lead to negligible differences in the aerodynamics. To this end, Fig. 6 enables one to consider a range of the small-scale energy of $E_S \pm \Delta E_{S,max}$, instead of a single set of target turbulence parameters. This is of practical importance due to the challenges related to wind tunnel testing for large model scales.

Using Eqn. (17), the interdependence of α and $\Delta E_{S,max}$ for different levels of E_S can be examined. Fig. 7 shows that for the same level of $\Delta E_{S,max}$, terrains with higher turbulence levels should have a lower α. For example, considering $\Delta E_{S,max} = 0.5 \times 10^{-3}$ and a terrain simulating a turbulence level of $E_S = 1 \times 10^{-3}$, the mismatch of integral length scales should be less than a ratio of 2.9, which is similar to the ASCE 49-21 (2021) recommendation. However, for the same level of $\Delta E_{S,max}$ but with a $E_S = 4.5 \times 10^{-3}$, the mismatch of integral length scales should be less than a factor of 1.3, which is less than half the recommended value of ASCE 49-21 (2021).

In addition to the mismatch of integral length scales, we consider the effects of a mismatch in the Jensen number on small-scale energy. Using Eqn. (14) and the atmospheric boundary layer model from ESDU 74 (1975), the interdependence of α_{zo} and $\Delta E_{S,max}$ for different levels of z_o are shown in Fig. 8. Fig. 8 shows that α_{zo} for suburban terrains, $z_o = 0.3$m, should be less than an open terrain, $z_o = 0.01$m for any range of $\Delta E_{S,max}$. The range of values for α_{zo} are less than 1.3 for $\Delta E_{S,max} < 1 \times 10^{-3}$, which is significantly stricter than the recommended mismatch of a factor of 3 in ASCE 49-21 (2021). This observation is because a mismatch of higher roughness length equates to a much larger turbulence intensity change, drastically shifting the vertical spectra and, subsequently, the small-scale energy.

These results highlight the importance of quantifying turbulence effects in terms of the proposed small-scale energy, E_S. Furthermore, the quantification of $\Delta E_{S,max}$ plays a critical role in relaxing the limits of PTS applications without allowing for altered aerodynamics. Below, recommendations of $\Delta E_{S,max}$ will be made based on an investigation of the effects of E_S on the pressure fluctuations. For the mean pressure field,

Table 1
Test conditions for TTU models in full and model-scale.

Test Characteristics	Full-Scale	Case 1	Case 2	Case 3	Case 4	Case 5	Case 6
Turbulence intensity, I_u	0.216	0.099	0.123	0.123	0.150	0.186	0.214
Integral length scale, L_u/H	8.84	3.7	7.5	4.9	8.8	5.1	7.6
Mean wind speed, $\bar{u}$ (m/s)	7.66	10.47	11.69	10.25	10.68	9.34	8.94
Small-scale energy, E_S	0.0030	0.0012	0.0013	0.0016	0.0018	0.0035	0.0038
Large-scale energy, E_L	0.00086	0.00019	0.00025	0.00030	0.00035	0.00065	0.00075

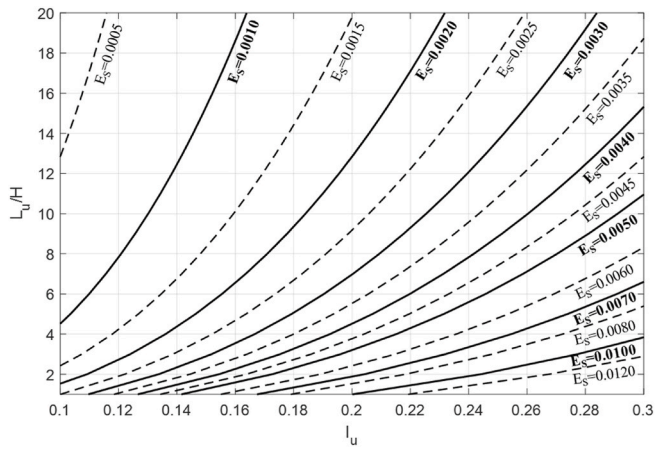

Fig. 6. Small-scale energy, E_S, as a function of typical ranges of turbulence intensity and integral length scales produced in a boundary layer wind tunnel.

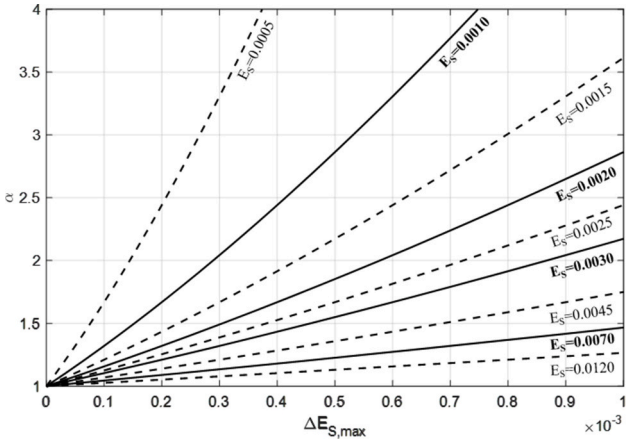

Fig. 7. Maximum allowable mismatch of integral length scales, α, as a function of the maximum allowable deviation of small-scale energy, $\Delta E_{S,max}$ considering various levels of small-scale turbulence, E_S.

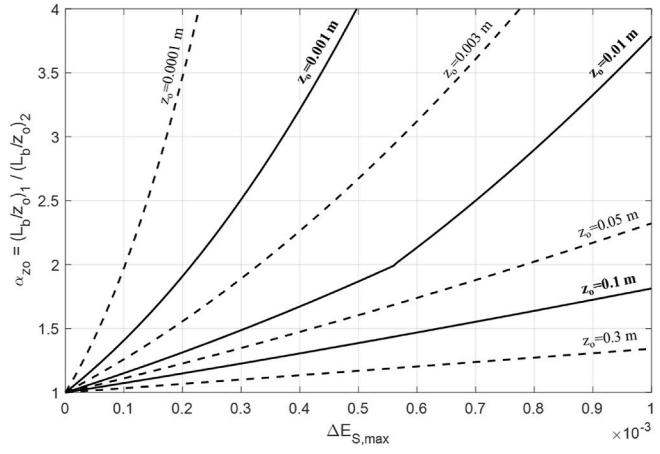

Fig. 8. Maximum allowable mismatch of integral length scales, α_{zo}, as a function of the maximum allowable deviation of small-scale energy, $\Delta E_{S,max}$ considering various levels of roughness length, z_o.

quantifying the effects of E_S on the change in the pressure field may be done by examining point pressures along the centerline of the roof. Meanwhile, for the parameters related to the pressure fluctuations, the analysis focuses on panel configurations due to the reliance of the quasi-steady pressure decomposition framework on area averages (Wu and Kopp, 2016, 2018; Guo et al., 2021).

4.2. Effect on mean pressure field

Akon and Kopp (2016) and Morrison and Kopp (2018) examined the mean pressure distribution along a centerline as a function of upstream turbulence conditions. To reconsider these data sets, the small-scale energy, E_S, is used to examine the trend of the combined effects of turbulence intensity and integral length scales. Fig. 9 shows C_p^* as a function of the distance x, normalized by the roof height, H. Each roof centerline plot with a different color (white to dark red) corresponds to varying levels of small-scale energy, as shown by the colour bar. Fig. 9 shows how the centerline plot shifts to the left with increasing E_S. The observation of Hillier and Cherry (1981), where the minimum mean pressure coefficient, $C_{p,min}$, occurs further away from the leading edge, is for ranges of $E_S < 1.5 \times 10^{-3}$. No significant changes in the mean pressure field are particularly observed when $E_S > 1.5 \times 10^{-3}$, particularly for point pressures at a distance $x/H < 0.5$. The dependency of the mean pressure field on E_S is further highlighted by examining the variation of the magnitude of the minimum mean pressure, $C_{p,min}$, location of the minimum pressure, x_{min}/H, and the reattachment length, x_r/H.

The location of $C_{p,min}$ with respect to the leading edge, x_{min}/H, is plotted against E_S in Fig. 10a. Here, it can be observed that x_{min}/H varies non-linearly for $E_S < 1.0 \times 10^{-3}$. For this range of E_S, the addition of small-scale energy significantly alters the initial flow development of the separating shear layer, and there will be significant changes in the mean pressure field from the leading edge of the roof up until the location of x_{min}/H. It is in this range of E_S where Lander et al. (2016) observed that Kelvin-Helmholtz (K-H) vortices emerge as the shear layer develops. Akon and Kopp (2018) suggest that the alteration of the development of the initial flow with increasing turbulence levels is caused by the K-H instability being suppressed in atmospheric boundary layer flows. It will also be in this range of E_S where a nonlinear relationship between the velocity and pressure spectra in the active scales will be observed (Morrison and Kopp, 2018). However, for higher levels of incident turbulence, larger-scale vortices exist prior to separation instead of the pairing of vortices through the K-H instability. Above a critical level of turbulence, the effects of turbulence on the development of the separating shear layer are saturated and would have minimal impact on the aerodynamic mechanisms (Akon and Kopp, 2018). The current results suggest that this saturated state of turbulence, at least with respect to the mean profiles, occurs for $E_S > 1.0 \times 10^{-3}$ where x_{min}/H is generally constant at 0.41H.

Fig. 10b shows the reattachment length, x_r/H, varying with E_S. The same trend of x_{min}/H with E_S is observed for x_r/H. Wu et al. (2017) showed that the increase of the recovery rate of mean pressure (or decrease of x_r/H) with turbulence is due to the significant contribution of Reynold's normal stresses to the total mean pressure gradient. Given that E_S may be a proxy for Reynold's normal stresses in the region of separated flow, the results are consistent with the findings of Wu et al. (2017). It can also be observed that the rate of decrease for x_r/H is greater than x_{min}/H, particularly for $E_S > 1.0 \times 10^{-3}$. Wu et al. (2017) discuss that it is the lack of turbulence-induced pressure gradients at higher turbulence levels that cause the difference of the rate of decrease for x_r/H. This leads to the dissimilarity of the reduced pressure coefficient for $x/H > 0.41$ (Akon and Kopp, 2016). Although the mean pressure fields continually varies with increasing E_S, Fig. 10b also suggests that this is negligible for $E_S > 1.0 \times 10^{-3}$.

Fig. 10c shows that the magnitude of the $C_{p,min}$ increases with E_S. This is consistent with Akon and Kopp (2016) who showed that the magnitude of $C_{p,min}$ increases with turbulence intensity. Since the turbulence intensity increases with the small-scale energy exponentially, the $C_{p,min}$ varies non-linearly with E_S as well. The variation of $C_{p,min}$ with

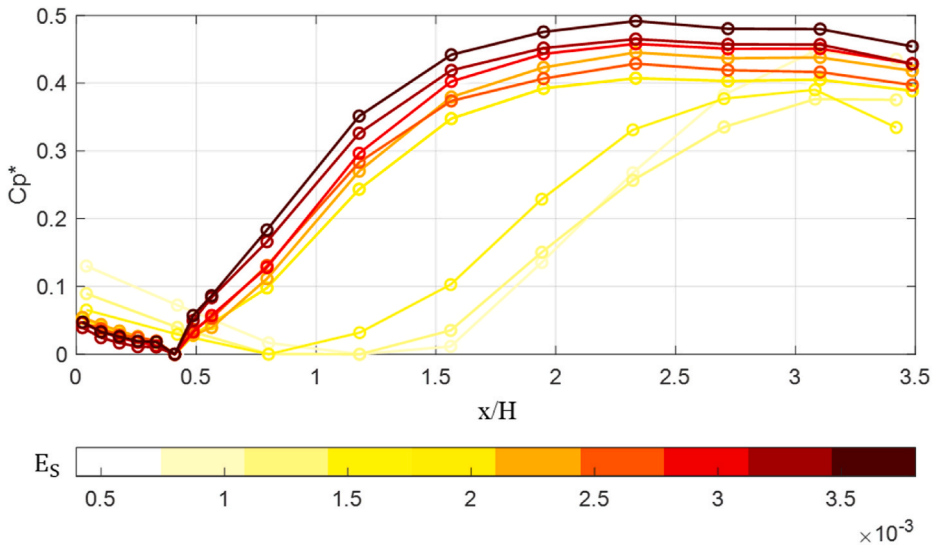

Fig. 9. Reduced pressure coefficient, Cp*, as a function of distance from the leading edge, x/H, and small scale energy, E_S, for point pressures along the centerline of the roof.

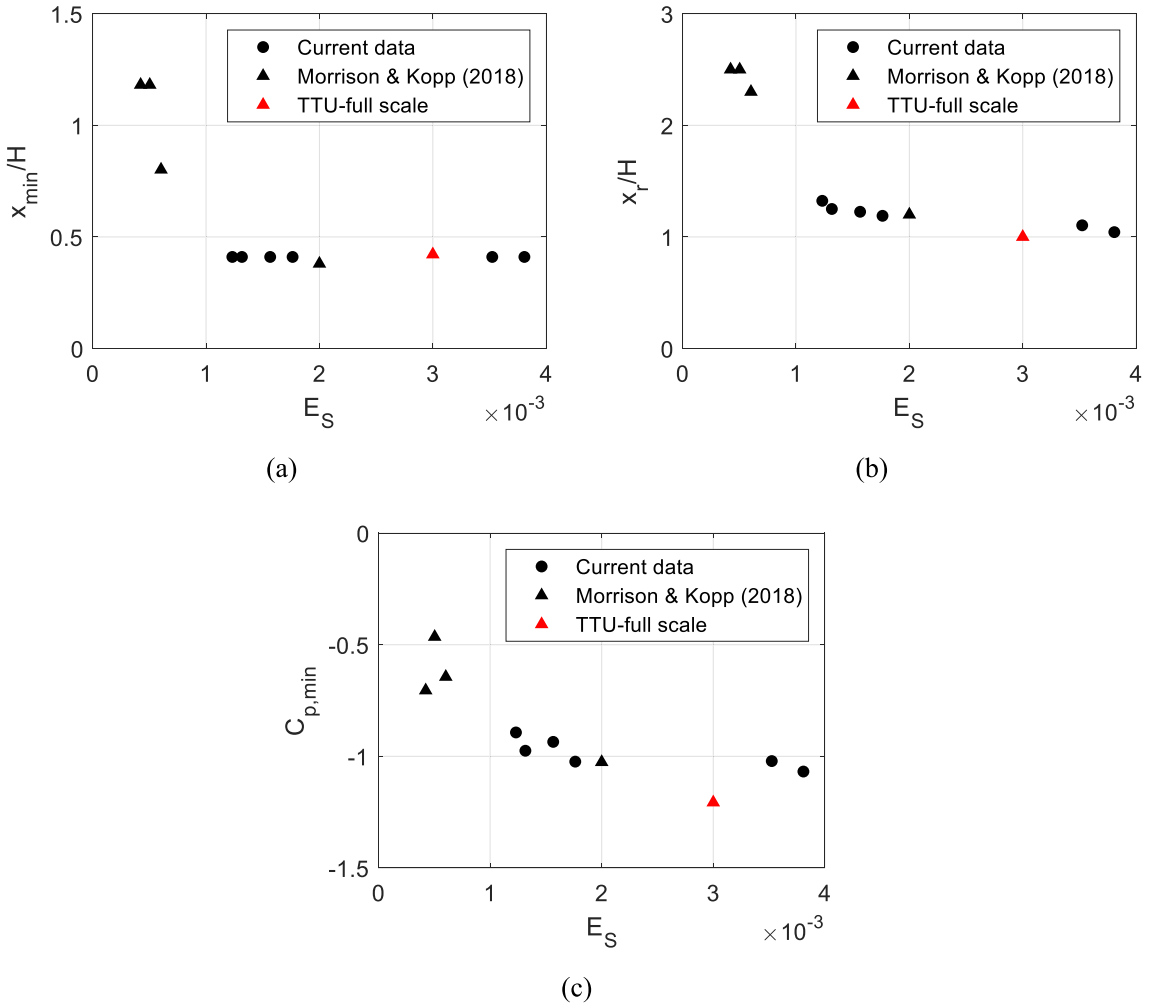

Fig. 10. (a) Location of the minimum mean pressure coefficient, x_{min}/H, (b) reattachment length, x_r/H, and (c) Minimum mean pressure coefficient, $C_{p,min}$, as a function of E_S.

respect to E_S further reduces for $E_S > 1.5 \times 10^{-3}$, wherein the differences may also be attributed to measurement uncertainty (Quiroga Diaz, 2006). Thus, the results imply that the constraint of PTS, which requires negligible changes in the aerodynamics, is most likely satisfied when $E_S > 1.5 \times 10^{-3}$. It should be noted that E_S only implicitly accounts for the effects to the total mean pressure gradient. Further experiments need to be done to quantify the relationship between the E_S and the Reynold stresses in the region of separated flow.

To show the applicability to an extension of the PTS framework, the maximum allowable deviation, $\Delta E_{S,max}$, is determined using Eqn. (20) with the TTU full-scale data as reference and by fitting a linear trend over the current data. Among the three parameters examined, the largest variation with respect to E_S occurs for x_r/H. Limiting $\Delta x_r/H$ to a maximum relative difference of 15% from the TTU measurement, $\Delta E_{S,max} < 5 \times 10^{-4}$ for the mean pressure field to be relatively the same and within uncertainty measurements. Thus, a wind tunnel simulation must target energy levels between 2.5×10^{-3} and 3.5×10^{-3} to minimize the differences in the mean pressure field of the roof of the full-scale TTU building.

4.3. Effects on pressure fluctuation energy

To examine the fluctuating pressure field, a pressure decomposition is needed. Here, Eqn. (24) & Eqn. (25) are used. These are validated against the quasi-steady pressure decomposition utilized by Guo et al. (2021). A high pass filter with a cut-off frequency of $0.1\bar{u}/H$ was applied to the high-frequency pressure signal derived using Eqn. (35). The comparison of the pressure spectra between the measured pressure signal and the calculated QS low (Eqn. (31)) and high-frequency pressure (Eqn. (35)) signals for panel C-4 are shown in Fig. 11. As can be seen, the QS model is successfully able to recreate the low-frequency pressure spectra.

Using the QS pressure decomposition, the nondimensional energy of the low and high-frequency pressure fluctuations are plotted against the corresponding large and small-scale energy in Fig. 12. The dashed 45-degree line shows Eqn. (24) and Eqn. (25) with $\beta_L = \beta_S = 1.0$. Fig. 12a shows that $\beta_L \approx 1.0$ for all the panel configurations, implying that the total large scale wind energy is fully transmitted to the area-averaged pressures (i.e., quasi-steady theory holds), regardless of area-averaging effects. However, in Fig. 12b, there is a reduction in the admittance, $\beta_S < 1.0$, of small-scale wind energy with increasing tributary area. This reduction of pressure energy is related to the rapid attenuation of higher frequencies, $\eta > 1.0$, associated with the filtering effects of area-averaging (Sharma and Richards, 2004; Wang and Kopp, 2023). β_S is close to one for panel C-4 due to this panel consisting of pressure taps just downstream of the leading edge, consistent with Wang and Kopp (2023) who showed that the aerodynamic admittance function for small-scales is close to one for point pressures near the leading edge. Additionally, Fig. 12b shows that the magnitude of β_S per panel

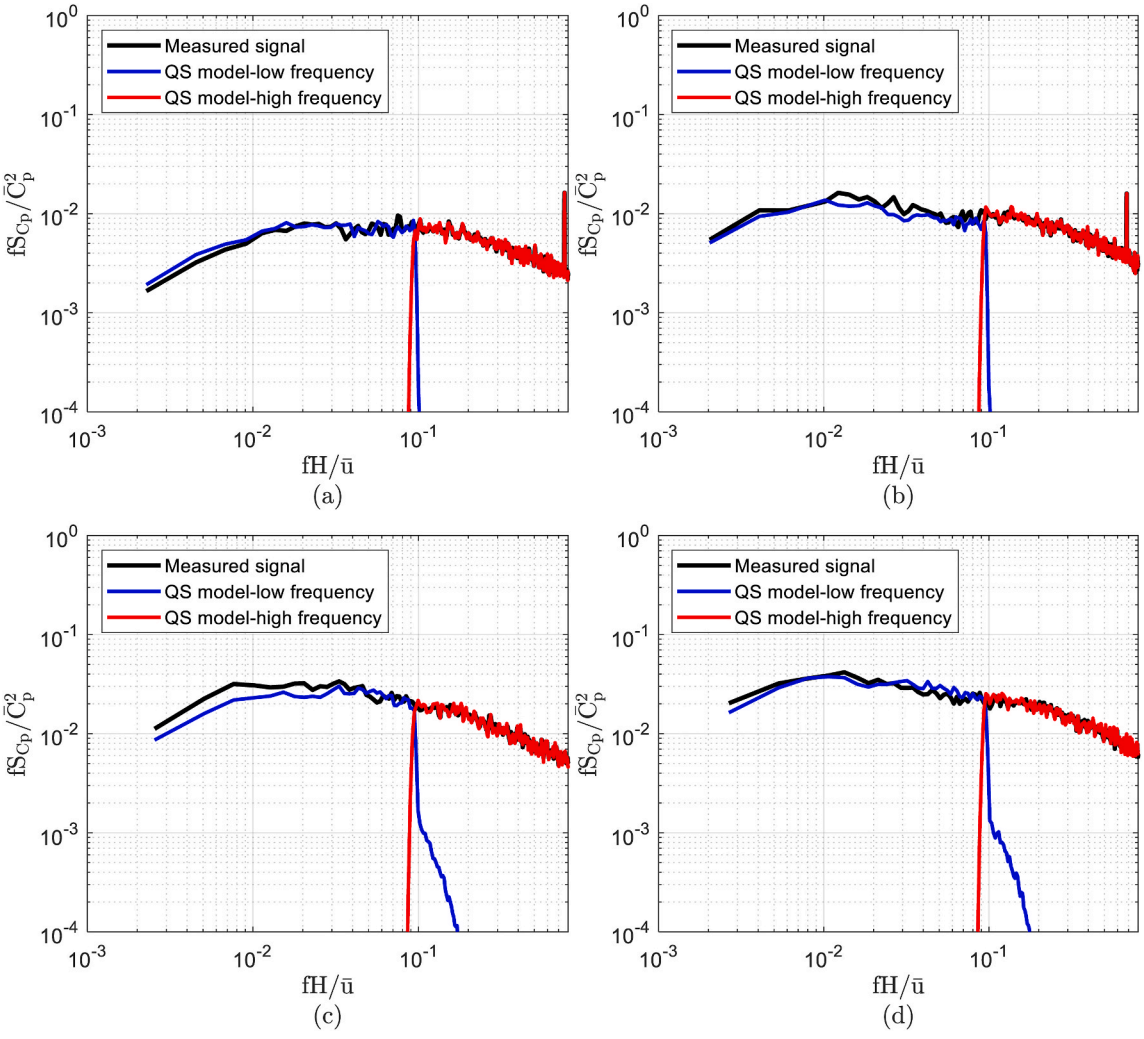

Fig. 11. Comparison of measured pressure signal with low and high frequency pressure signals modeled using the quasi-steady vector approach for panel C-4 with terrain case (a) 1, (b) 2, (c) 5, and (d) 6.

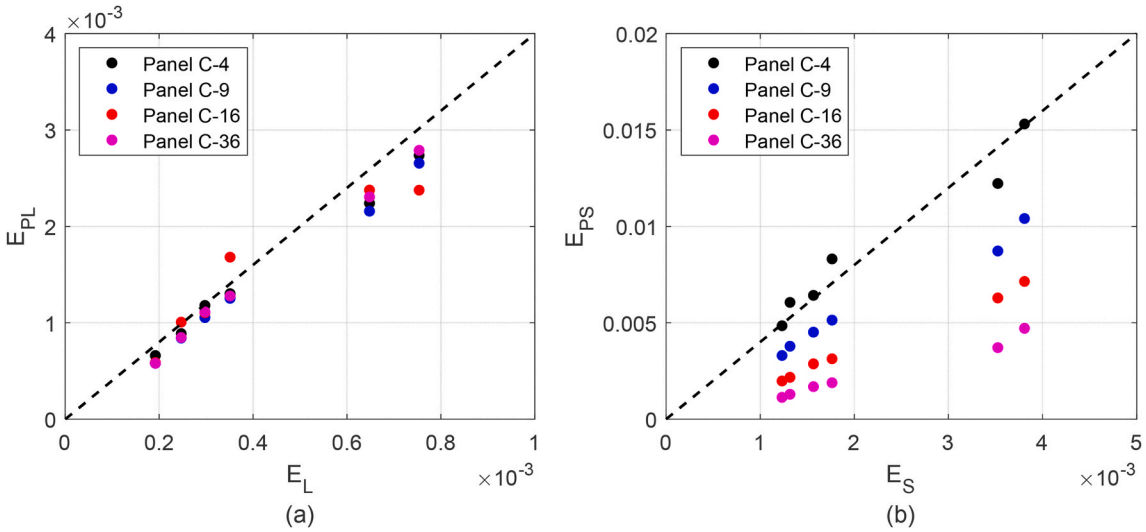

Fig. 12. Nondimensional pressure fluctuation energy for low (a) and high (b) frequency pressure fluctuations for panels C-4, C-9, C-16 and C-36 as a function of large and small scale energy, respectively.

configuration is relatively constant for different levels of small-scale energy, implying that the aerodynamic admittance function does not differ significantly across the terrains tested. The results show that in this range of turbulence, where suggested saturation effects of turbulence occur (Akon and Kopp, 2018), the pressure energy may be linearly corrected (Guo et al., 2021).

The recommended $\Delta E_{S,max}$ for an extension of PTS application to the TTU building can be determined based on the nondimensional pressure energy. Given that a linear relationship exists, as shown in Fig. 12a and b, Eqn. (20) can be re-written as

$$\Delta E_{S,max} = 0.15 E_S \tag{39}$$

For the TTU building with a target $E_S = 3 \times 10^{-3}$, $\Delta E_{S,max}$ should be less than $\approx 5 \times 10^{-4}$. Thus, a wind tunnel simulation must target energy levels between 2.5×10^{-3} and 3.5×10^{-3} to have the same pressure energy levels as the full-scale target of TTU. Comparing the recommended $\Delta E_{S,max}$ based on the mean pressures, from the previous section, and the pressure energy, the $\Delta E_{S,max}$ based on pressure energy will always govern when turbulence effects on the separating shear layer are saturated. Thus, Eqn. (39) is a reasonable approach to determine $\Delta E_{S,max}$ for $E_S > 1.5 \times 10^{-3}$.

4.4. Effects on crossing rates

Fig. 13 shows the contribution of both small and large-scale energy to the total normalized crossing rate defined in Eqn. (29) and Eqn. (30). Several observations can be made from the analysis. First, the comparison between Fig. 13a–b indicates that the contribution of large-scale energy is negligible compared to that of small-scale energy. Specifically, low-frequency pressure fluctuations, $\eta < 0.10$, account for less than 3.5% of the total crossing rate for panel C-36. The contribution becomes less than 1% for tributary areas smaller than panel C-4. This implies that matching the small-scale energy for PTS application accounts at least 97% of the total normalized crossing rate in this region of separated flow.

The trend of the crossing rate is similar to nondimensional pressure fluctuation energy, wherein the same linear trend can be observed for small-scale energy. Thus, due to the zero intercept, $\Delta E_{S,max}$ is independent of the panel tributary area and should also be less than $\approx 5 \times 10^{-4}$. In Fig. 13a, the slope reduction with increasing area average is related to the attenuation of higher-pressure frequencies. A similar formulation related to Eqn. (25) may be derived in future work wherein the slope is a function of β_S, with the tributary area being considered. This may be

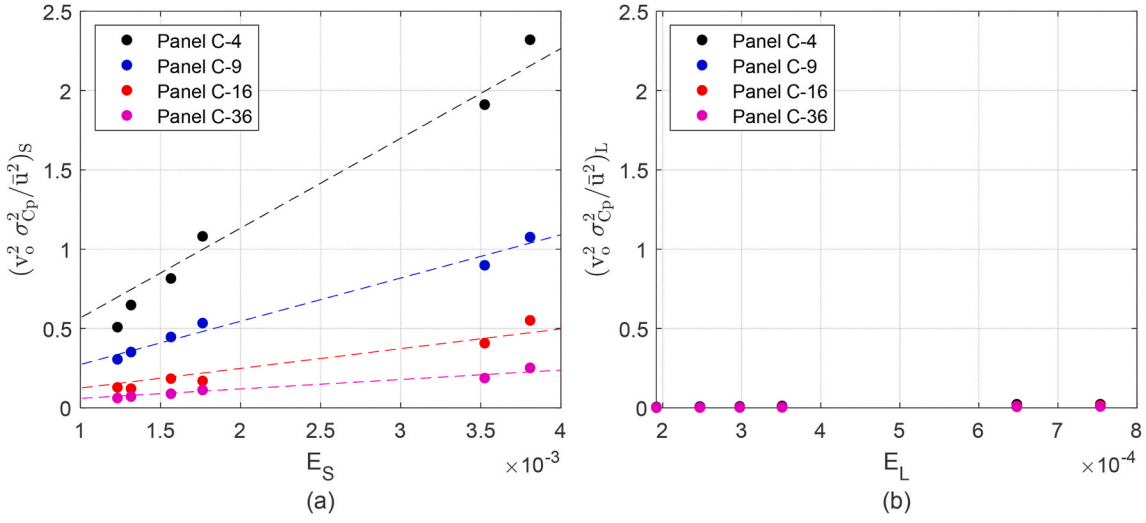

Fig. 13. (a) Contribution of small-scale energy, E_s, and (b) large-scale energy, E_L, to the up-crossing rate for panels C-4, C-9, C-16, and C-36.

useful for corrections of the crossing rate using a linear approach.

4.5. Statistical distributions

The skewness and kurtosis of low and high-frequency pressure fluctuations for the four panel configurations are determined. Fig. 14a–b shows the skewness of low-frequency and high-frequency pressure fluctuations, respectively. Fig. 14c–d shows the kurtosis of high-frequency and low-frequency pressure fluctuation. Several observations can be made. The first interesting observation is that the skewness and kurtosis of the low-frequency pressure fluctuations collapse regardless of the panel size. Additionally, the results show that the low-frequency pressure fluctuations have a negatively skewed distribution (Fig. 14a) but with a short tail and kurtosis close to 3 (Fig. 14c). The fluctuations do not follow a Gaussian distribution despite the oncoming wind velocity fluctuations assumed to follow a Gaussian or near Gaussian distribution (Chu et al., 1996; Lu and Porte-Agel, 2010; Asghari-Mooneghi et al., 2016). Additionally, it is observed that both skewness and kurtosis increase with E_L until $E_L \approx 3.5 \times 10^{-4}$. These higher-order statistics then plateau at constant magnitudes for $E_L > 3.5 \times 10^{-4}$. Although not shown here, the Cobra probe velocity measurements show an increase in positive skewness with increasing large-scale energy. Using a quadrant analysis, Fernández-Cabán and Masters (2018) showed that rougher terrains, with higher positive skewness near the ground surface, are linked to the dominance of sweep events. Thus, the results suggest that the skewness of low-frequency pressure fluctuations on the roof are dependent on large-scale energy, which is related to large-scale coherent structures in the wind. Further work is needed to quantify this dependence. Lastly, these results suggest that for $E_L < 3.5 \times 10^{-4}$, an associated correction on the peak factor must be considered.

On the other hand, Fig. 14b–d shows that the high-frequency pressure fluctuations are a function of the tributary area. The skewness approaching zero with a higher tributary area emphasizes the spatial filtering effect that reduces the non-Gaussianity. The skewness is also observed to be invariant of the small-scale energy. However, kurtosis, which significantly contributes to the peak factor (Liu et al., 2017), increases with E_S (Fig. 14d). This result indicates that the distribution of the peaks is continuously driven by small-scale energy. To further emphasize the effects of turbulence, the tail distribution of the total instantaneous peak factor, $g_p(t)$, for the four panel configurations is shown in Fig. 15. Generally, there is a longer tail distribution with an increase of E_S when $E_S < 1.5 \times 10^{-3}$. For $E_S > 1.5 \times 10^{-3}$, the tail distributions appear to collapse on top of each other, especially for panels C-16 and C-36. This translates into an almost constant peak factor. This trend aligns with the effects of turbulence on the normalized mean pressure coefficient, where turbulence saturation effects are observed for $E_S > 1.5 \times 10^{-3}$. Thus, the paper suggests that the minimum should be $E_S > 1.5 \times 10^{-3}$ for PTS to better approximate peaks.

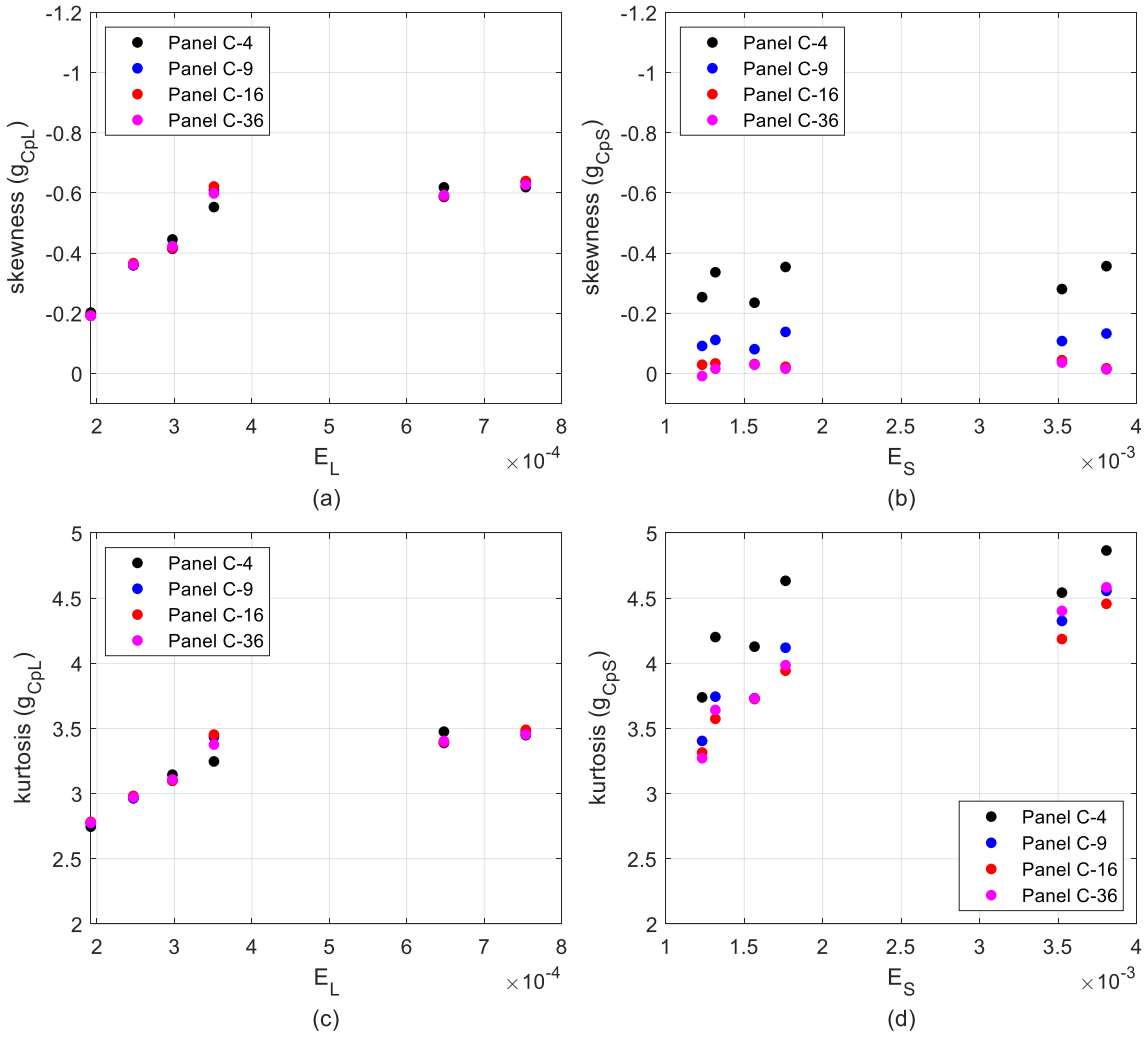

Fig. 14. (a & b) Skewness and (c & d) kurtosis for low, $g_{Cp,L}$, and high frequency, $g_{Cp,S}$, fluctuations, respectively, for four panel configurations.

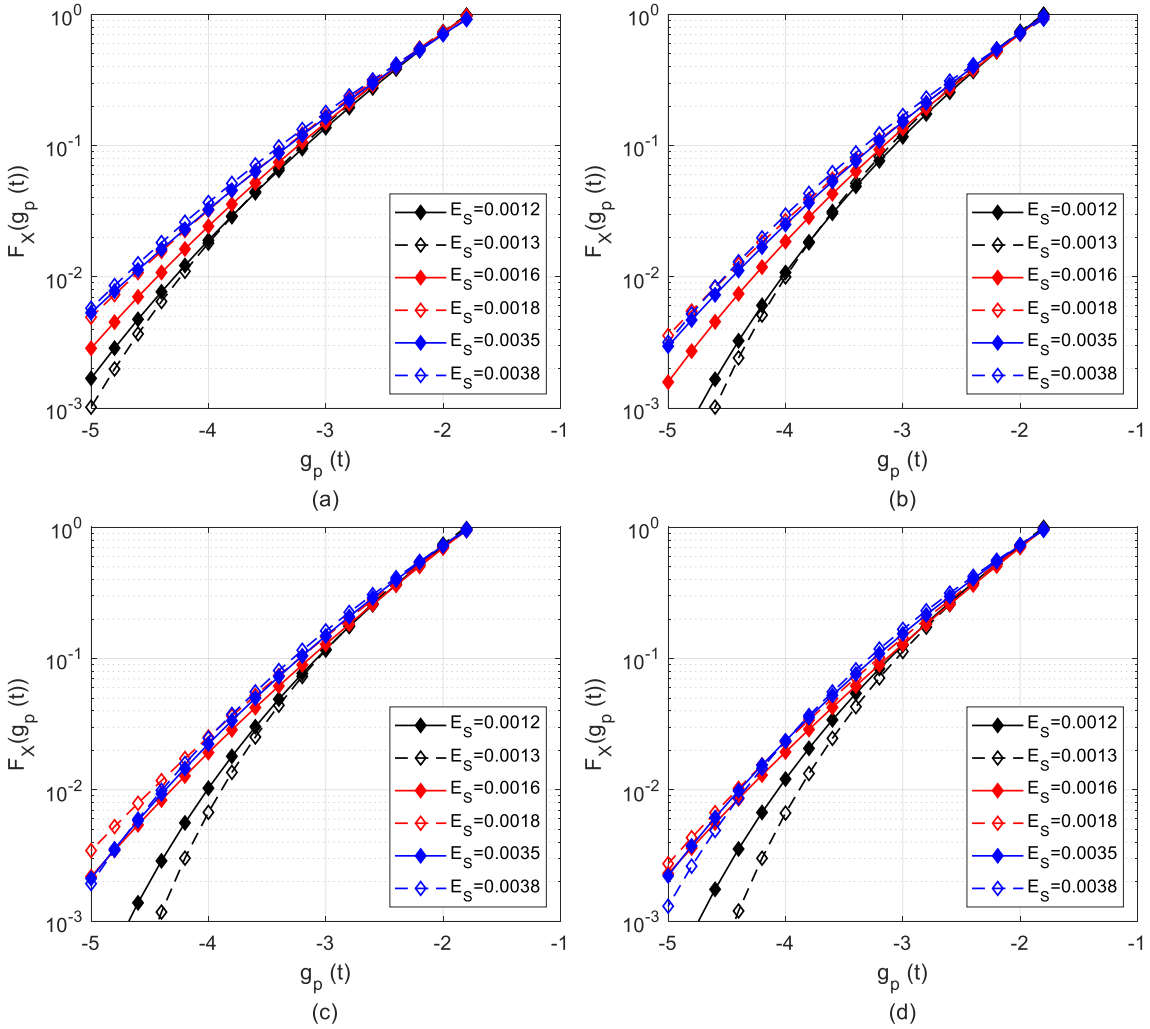

Fig. 15. Tail distribution as affected by small-scale energy, E_S, for panel configuration (a) C-4, (b) C-9, (c) C-16, and (d) C-36.

4.6. Region of saturated effects of turbulence

Based on the previous sections, the results suggest that there is a lower threshold for small and large-scale energy such that their effects are saturated for the mechanisms of the separating-reattaching shear layer on the roof. Given $E_S > 1.5 \times 10^{-3}$ and $E_L > 3.5 \times 10^{-4}$ and by using Eqn. (4) and Eqn. (5), a region can be plotted where any pair of turbulence intensity and integral length scales will result in saturated effects of turbulence for the TTU building. Fig. 16 highlights the suggested region in a green colour. This suggests that for the TTU building considered, a post-test correction of the large-scale energy effects based on a PTS approach will only be applicable for the green region. For the white region in Fig. 16, there may be non-linear variations in the mean pressure field with a reduction of integral length scales, which invalidates the constraint of PTS to not alter the aerodynamic effects. However, it should be noted that for $E_S > 1.5 \times 10^{-3}$ but $E_L < 3.5 \times 10^{-4}$, PTS may still be applicable given that the full-scale time history is available to account for the variation in the statistics of low-frequency wind fluctuations. Further research is needed to examine how this region of saturated turbulence effects varies with different building geometries. Additionally, the lower threshold limits may vary depending on the aerodynamic mechanism being investigated, which merits the need for more experimental data, particularly for $E_S < 1.5 \times 10^{-3}$, where the aerodynamics may to vary significantly with small increments of small scale energy.

To illustrate how the small-scale energy and corresponding spectra

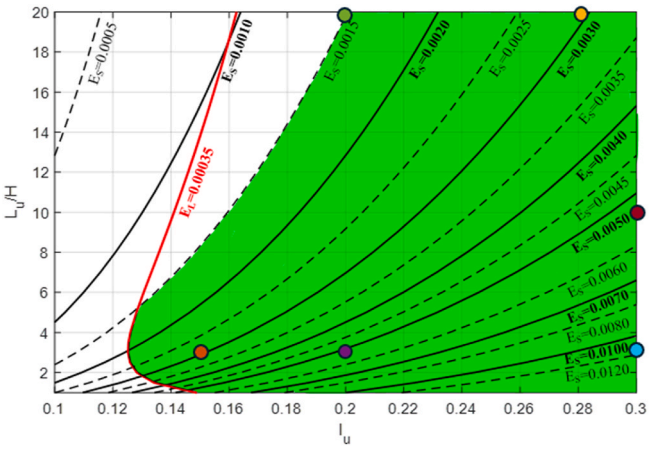

Fig. 16. Small-scale energy, E_S, as a function of typical ranges of turbulence intensity and integral length scales with a proposed region of saturated effects of turbulence.

vary within the proposed region of saturated effects of turbulence, Fig. 17 shows spectra for six selected pairs of turbulence intensity and integral length scales and the full-scale target spectra for TTU. To highlight the shift of the spectra with respect to the target TTU data, two points are selected at the ends of the bold black line, for $E_S = 3 \times 10^{-3}$,

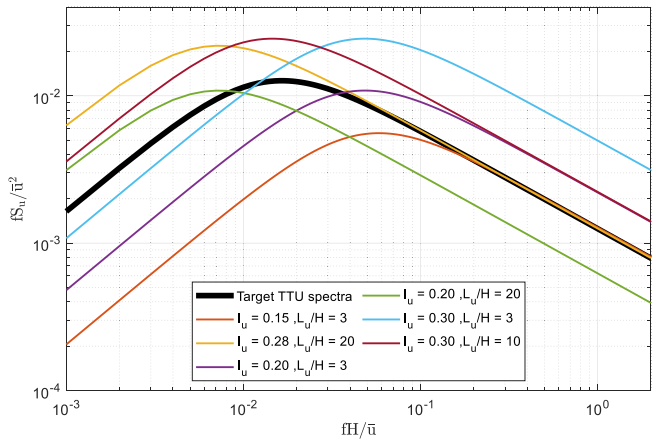

Fig. 17. Power spectral density for different pairs of turbulence intensity and integral length scales in the region of saturated turbulence.

shown in Fig. 16. The first point corresponds to a $I_u = 0.15$ and $L_u/H = 3$ while the second point corresponds to $I_u = 0.28$ and $L_u/H = 20$. The spectra within the active scales, $0.1 \leq \eta \leq 2$, match really well, as expected. However, it should be noted that spectra representing the first point has a small mismatch near $\eta = 0.1$ when compared to the full-scale target spectrum of TTU. The full-scale target spectrum has higher energy for $\eta < 0.2$. These scenarios only occur for low magnitudes of integral length scales.

Four spectra are also shown in Fig. 17 to illustrate how the integral length scale shifts the spectra. For a case with $I_u = 0.20$ and $L_u/H = 3$ (purple line), the small-scale energy is $E_S = 5 \times 10^{-3}$ which is three times more than the small-scale energy for the case with $I_u = 0.20$ and $L_u/H = 20$ (green line), which is at the limit for the recommended region of saturated effects of turbulence. However, for a $I_u = 0.30$, a shift of $L_u/H = 3$ (blue line) to $L_u/H = 10$ (blue line) almost halves the small-scale energy but maintains the small-scale energy to be within a region of saturated effects of turbulence.

5. Conclusions

The paper proposes small-scale and large-scale turbulence energy parameters to simultaneously encompass the effects of turbulence intensity and integral length scales on the active scales of turbulence, which control the aerodynamics of regions of separated-reattaching flow. The mathematical formulation arises by renormalizing the von Karman wind spectra and accounting for turbulence intensity and integral length scales. The small-scale energy is determined by integrating the renormalized spectra from a nondimensional frequency of 0.1–2, which is the frequency range that captures the nonlinear relationships between velocity and pressure fluctuations. The large-scale energy is determined by integrating for a nondimensional frequency less than 0.1.

The small-scale energy parameter is particularly useful in PTS applications. Given that there are minimal changes to the aerodynamic behavior, a maximum allowable deviation of small-scale energy can be quantified. This results in a broader range of turbulence parameters that may be considered for simulating a target small-scale energy in an atmospheric boundary layer wind tunnel. Furthermore, using the proposed small-scale energy parameter highlights how an increase of the integral length scales shifts the wind spectra and corresponding influences the active scales of turbulence. The effect of integral length scales on small-scale energy may go up to an order of magnitude higher in rough terrains than in smoother terrains with lower turbulence levels. With this concept, the paper proposes that the maximum allowable mismatch of integral length scales and aerodynamic roughness lengths in wind tunnel test provisions should depend on turbulence levels and the maximum allowable deviation of small-scale energy, which is set by considering the measurement uncertainty.

The paper proposes an equation for the equivalent turbulence parameters for a model scale test that matches full-scale turbulence conditions, considering a maximum allowable deviation in the total small-scale energy. This limit is determined by assessing when variations in small-scale energy have negligible influence on mean values, pressure variances, and the statistical distributions. The paper examines the maximum allowable mismatch in small-scale energy for the separating shear layer above the roof of several turbulent cases of the TTU building. The investigation reveals that minimum mean pressure coefficients and peak factors exhibit exponential trends at small-scale energy levels below $E_{S=1.5} \times 10^{-3}$, plateauing after that, indicating saturation effects of small-scale turbulence. Moreover, the nondimensional pressure energy related to high-frequency pressure fluctuations displays a linear relationship with small-scale energy, a trend consistent across the panel configurations examined.

Using a CDF mapping translation framework with quasi-steady pressure decomposition, the analysis reveals that the crossing rate and kurtosis significantly contribute to the peak and are highly dependent on small-scale energy. The analysis also shows that the low-frequency pressure fluctuations are non-Gaussian, wherein the statistical distribution becomes more negatively skewed with increasing large-scale energy until a certain limit. For large-scale energy levels above $E_{L=3.5} \times 10^{-4}$, the skewness appears to plateau. These results imply that a minimum integral length scale limit should also be established for post-test corrections using PTS to remain plausible. Further research must be conducted to investigate the relationship between sweep dominant events, large-scale energy, and the skewness of low-frequency pressure fluctuations.

Lastly, the paper proposes a framework that can identify a region of saturated effects of turbulence. Corrections based on a PTS approach no longer apply for turbulent cases outside the identified region due to the non-linear variation of the mean pressure field and the statistics of the low frequency pressure fluctuations. The observed trends may also be improved by incorporating the effects of vertical turbulence, which also affects the pressure fluctuations on the roof. The same framework discussed in this paper may be applied to examine the effects of small-scale energy on other aerodynamic mechanisms, such as conical vortices and vortex shedding.

Future work should also examine the applicability of the framework to different peak loads, such as drag, where different surfaces on the building respond to different aerodynamic mechanisms (e.g., for drag, both the windward and leeward walls). Finally, the limits for the region of saturated effects of turbulence may also vary for different building geometries, and for smaller non-engineering structures and building components, such as rooftop appurtenances and roofing components. Further experimental data is needed to investigate a general limit that encompasses a wide range of buildings and components. Other research needs related to these topics, such as examining Reynolds number effects, have been discussed by Kopp (2023).

CRediT authorship contribution statement

Timothy John Acosta: Writing – review & editing, Writing – original draft, Validation, Methodology, Investigation, Formal analysis, Data curation, Conceptualization. **Yitian Guo:** Writing – review & editing, Methodology, Data curation, Conceptualization. **Jin Wang:** Writing – review & editing, Supervision, Methodology, Formal analysis, Conceptualization. **Stefano Brusco:** Writing – review & editing, Formal analysis, Conceptualization. **Gregory A. Kopp:** Writing – review & editing, Supervision, Methodology, Funding acquisition, Formal analysis, Conceptualization.

Declaration of competing interest

The authors declare that they have no known competing financial interests or personal relationships that could have appeared to influence the work reported in this paper.

Data availability

Data will be made available on request.

Acknowledgements

GAK gratefully acknowledges the partial financial support provided by the NSERC Discovery Grants program. TJA gratefully acknowledges the financial support of the Philippine Department of Science and Technology - Science Education Institute.

References

Acosta, T.J., Wang, J., Kopp, G.A., 2024. Non-Gaussian peak factor model for windward walls of rigid buildings of different aspect ratios. J. Wind Eng. Ind. Aerod. 245, 105654.
Akon, A.F., Kopp, G.A., 2016. Mean pressure distributions and reattachment lengths for roof-separation bubbles on low-rise buildings. J. Wind Eng. Ind. Aerod. 155, 115–125.
Akon, A.F., Kopp, G.A., 2018. Turbulence structure and similarity in the separated flow above a low building in the atmospheric boundary layer. J. Wind Eng. Ind. Aerod. 182, 87–100.
ASCE, 2021. Wind Tunnel Testing for Buildings and Other Structures, ASCE 49-21. American Society of Civil Engineers, Reston, VA, USA.
Asghari-Mooneghi, M., Irwin, P., Gan Chowdhury, A., 2016. Partial turbulence simulation method for predicting peak wind loads on small structures and building appurtenances. J. Wind Eng. Ind. Aerod. 157, 42–62.
Banks, D., 2011. Measuring peak wind loads on solar power assemblies. In: Proceedings of the 13th International Conference of Wind Engineering. Amsterdam, the Netherlands, July.
Banks, D., 2013. The role of corner vortices in dictating peak wind loads on tilted flat solar panels mounted on large, flat roofs. J. Wind Eng. Ind. Aerod. 123, 192–201.
Bearman, P.W., Morel, T., 1983. Effect of free stream turbulence on the flow around bluff bodies. Prog. Aero. Sci. 20 (2–3), 97–123.
Braun, R., Chen, D., Chowdhury, A., Estephan, J., Gordon, C., Irwin, P., et al., 2021. Peak Wind Effects on Low-Rise Building Roofs and Rooftop PV Arrays. 6th American Association Wind Engineering Workshop, Clemson, SC, USA, 2021.
Estephan, J., Chowdhury, A.G., Irwin, P., 2022. A new experimental-numerical approach to estimate peak wind loads on roof-mounted photovoltaic systems by incorporating inflow turbulence and dynamic effects. Eng. Struct. 252, 113739.
Chu, C.R., Parlange, M.B., Katul, G.G., Albertson, J.D., 1996. Probability density functions of turbulent velocity and temperature in their atmospheric surface layer. Water Resour. Res. 1681–1688.
ESDU, 1975. Characteristics of Atmospheric Turbulence Near the Ground. Part II: Single Point Data for Strong Winds (Neutral Atmosphere). Engineering Science Data Unit 74031. London, England.
Fernández-Cabán, P.L., Masters, F.J., 2018. Effects of freestream turbulence on the pressure acting on a low-rise building roof in the separated flow region. Frontiers in the Built Environment 4, 17.
Ginger, J.D., Letchford, C.W., 1993. Characteristics of large pressures in regions of flow separation. J. Wind Eng. Ind. Aerod. 49 (1–3), 301–310.
Grigoriu, M., 1995. Applied Non-gaussian Processes: Examples, Theory, Simulation, Linear Random Vibration, and MATLAB solutions(Book). Prentice Hall, Inc, Englewood Cliffs, NJ, 1995.
Guo, Y., Wu, C.H., Kopp, G.A., 2021. A method to estimate peak pressures on low-rise building models based on quasi-steady theory and partial turbulence analysis. J. Wind Eng. Ind. Aerod. 218, 104785.
Hillier, R., Cherry, N.J., 1981. The effects of stream turbulence on separation bubbles. J. Wind Eng. Ind. Aerod. 8, 49–58.
Ho, T.C.E., Surry, D., Morrish, D., Kopp, G.A., 2005. The UWO contribution to the NIST aerodynamic database for wind loads on low buildings: Part 1. Archiving format and basic aerodynamic data. J. Wind Eng. Ind. Aerod. 93 (1), 1–30.
Irwin, P.A., 1998. The role of wind tunnel modelling in the prediction of wind effects on bridges. In: Proeedings. Of the International Symposium on Advances in Bridge Aerodynamics, pp. 99–117.
Irwin, P.A., 2008. Bluff body aerodynamics in wind engineering. J. Wind Eng. Ind. Aerod. 97 (6–7), 701–712.
Kareem, A., Wu, T., 2013. Wind-induced effects on bluff bodies in turbulent flows: nonstationary, non-Gaussian and nonlinear features. J. Wind Eng. Ind. Aerod. 122, 21–37.
Kopp, G.A., 2023. Updates to the wind tunnel method for determining design loads in ASCE 49-21. Wind Struct. 37 (2), 163–178.
Kwan, K., Kopp, G.A., 2021. The effects of edge radius on wind tunnel tests of low-rise buildings. J. Wind Eng. Ind. Aerodyn. 214, 104668.
Lander, D.C., Letchfold, C.W., Amitay, M., Kopp, G.A., 2016. Influence of the bluff body shear layers on the wake of a square prism in a turbulent flow. Physical Review Fluids 1, 044406.
Levitan, M.L., Mehta, K.C., 1992a. Texas Tech field experiments for wind loads part 1: building and pressure measuring system. J. Wind Eng. Ind. Aerod. 43, 1565–1576.
Levitan, M.L., Mehta, K.C., 1992b. Texas Tech field experiments for wind loads part II: meteorological instrumentation and terrain parameters.". J. Wind Eng. Ind. Aerod. 43, 1577–1588.
Moravej, M., Chowdhurry, A., Irwin, P., Zisis, I., 2018. Dynamic effects of wind loading on photovoltaic systems. In: Proceedings of the 14th International Conference of Wind Engineering. Porto Algre, Brazil.
Liu, M., Chen, X., Yang, Q., 2017. Estimation of peak factor of non-Gaussian wind pressures by improved moment-based Hermite model. J. Eng. Mech. 143 (7), 06017006.
Lu, H., Porte-Agel, F., 2010. A modulated gradient model for large-eddy simulation: Application to a neutral atmospheric boundary layer. Phys. Fluids 22, 015109.
Macdonald, J.H.G., Irwin, P.A., Fletcher, M.S., 2002. "Vortex-induced vibrations of the Second Severn Crossing cable-stayed bridge-full-scale and wind tunnel measurements. Ice: Struct. Build 123–124.
Morrison, M.J., Kopp, G.A., 2018. Effects of turbulence intensity and scale on surface pressure fluctuations on the roof of a low-rise building in the atmospheric boundary layer. J. Wind Eng. Ind. Aerod. 183, 140–151.
Peng, X., Yang, L., Gavanski, E., Gurley, K., Prevatt, D., 2014. A comparison of methods to estimate peak wind loads on buildings. J. Wind Eng. Ind. Aerod. 126, 11–23.
Quiroga Diaz, P.S., 2006. Uncertainty Analysis of Surface Pressure Measurements on Low-rise 636 Buildings. Master's thesis. The University of Western Ontario.
Rice, S.O., 1945. Mathematical analysis of random noise. The Bell System Technical Journal 24 (1), 46–156.
Roshko, A., Lau, J.C., 1965. Some observations on transition and reattachment of a free shear layer in incompressible flow. In: Proceedings of the Heat Transfer and Fluid Mechanics Institute.
Sadek, F., Simiu, E., 2002. Peak non-Gaussian wind effects for database-assisted low-rise building design. J. Eng. Mech. 128, 530–539.
Stathopoulos, T., Surry, D., 1983. Scale effects in wind tunnel testing of low buildings. J. Wind Eng. Ind. Aerod. 13, 313–326.
Sharma, R.N., Richards, P.J., 2004. The multi-stage process of windward wall pressure admittance. J. Wind Eng. Ind. Aerodyn. 92 (14–15), 1191–1218.
Tubino, F., Solari, G., 2020. Time varying mean extraction for stationary and nonstationary winds. J. Wind Eng. Ind. Aerodyn. 203, 104187.
Wang, J., Kopp, G.A., 2023. Gust effect factors for regions of separated flow around low-, mid-, and high-rise buildings. J. Wind Eng. Ind. Aerod. 232, 105254.
Wu, C.H., Kopp, G.A., 2016. Estimation of wind-induced pressures on a low-rise building using quasi-steady theory. Frontiers in Built Environement 2, 5.
Wu, C.H., Akon, A.F., Kopp, G.A., 2017. Effects of turbulence on the mean pressure field in the separating-reattaching flow above a low-rise building. J. Wind Eng. Ind. Aerod. 171, 79–92.
Wu, C.H., Kopp, G.A., 2018. A quasi-steady model to account for the effects of upstream turbulence characteristics on pressure fluctuations on a low-rise building. J. Wind Eng. Ind. Aerod. 179, 338–357.
Zhao, H., Grigoriu, M., Gurley, K.R., 2019. Translation processes for wind pressures on low-rise buildings. J. Wind Eng. Ind. Aerod. 184, 405–416.